



Full length article



Near-infrared-based determination of mass-based material flow compositions in mechanical recycling of post-consumer plastics: Technical feasibility enables novel applications

Nils Kroell^{a,*}, Xiaozheng Chen^a, Bastian Küppers^b, Julius Lorenzo^a, Abtin Maghmoumi^a, Matthias Schlaak^a, Eric Thor^a, Christian Nordmann^b, Kathrin Greiff^a

^a Department of Anthropogenic Material Cycles, RWTH Aachen University, Wuellnerstr. 2, D-52062, Aachen, Germany

^b STADLER Anlagenbau GmbH, Max-Planck-Str. 2, D-88361, Altshausen, Germany

ARTICLE INFO

Keywords:

Sensor-based material flow characterization
Sensor-based sorting
Automated quality control
Lightweight packaging waste
Machine learning
Circular economy

ABSTRACT

Mass-based material flow compositions (MFCOs) are crucial to assess and optimize mechanical plastic recycling processes. While MFCOs are determined by manual sorting analysis today, in the future MFCOs could be determined inline through near-infrared-based material flow characterization. This study aims to quantify the accuracy of near-infrared-based MFCO determinations to assess its technical feasibility. Binary mixtures of plastic flakes and post-consumer packaging were pixel-based classified at different material flow presentations, and mass-based MFCOs were predicted from the resulting false-color data using different data processing techniques. The results show high correlations between near-infrared-based false-color data and mass-based MFCOs. Through regression models and data aggregation, it was possible to predict mass-based MFCOs with mean absolute errors of 0.5% and 1.0% and R^2 -scores of 99.9% and 99.4% for plastic flakes and packaging, respectively, across all material flow presentations. The demonstrated technical feasibility thus paves the way for new sensor technology applications in plastic recycling.

1. Introduction

Since the invention of the first synthetic polymer in 1907 (Crespy et al., 2008), more than 8,300 Mt of plastics have been produced worldwide (Geyer et al., 2017). While advantageous material properties and low production costs of plastics have led to their widespread use in the first place, these advantages have recently been overshadowed by negative environmental impacts (Dris et al., 2020). Production of new plastic requires fossil fuels as raw material, consumes large amounts of energy, and emits significant amounts of greenhouse gases (GHGs) (Zheng and Suh, 2019); it is estimated that cumulative GHG emissions associated with plastics could account for 10% to 13% of the total remaining carbon budget by 2050 (Shen et al., 2020). In 2010 alone, about 4.8 million to 12.7 million tons of plastics entered the oceans (Jambeck et al., 2015), where they endanger wildlife (Moore, 2008) and accumulate as microplastics in organisms and food chains (Avio et al., 2017; Chen et al., 2021a).

The global plastics crisis can only be tackled through a plethora of complementary measures (Nielsen et al., 2020). Starting with the reduction of plastic consumption, through longer use cycles and reuse of plastic products to zero-loss collection and high-quality recycling, these measures contribute to a reduction of the environmental impacts of plastics. In this regard, recycling processes play a key role: On the one hand, plastic recycling avoids negative impacts of alternative end-of-life operations (e.g., incineration, landfilling). On the other hand, produced plastic recyclates can substitute primary plastics and thus avoid negative environmental impacts of primary plastic production (Cudjoe et al., 2021). Among all recycling processes, mechanical recycling is considered particularly advantageous due to its low energy demand and low carbon footprint (Davidson et al., 2021).

Abbreviations: BC, beverage carton; GHG, greenhouse gases; HDPE, high-density polyethylene; LWP, lightweight packaging waste; MAE, mean absolute error; MFCO, material flow composition; MFP, material flow presentation; MO, monolayer; MU, measurement uncertainty; NIR, near-infrared; PET, polyethylene terephthalate; RR, reduction ratio; SBMC, sensor-based material flow characterization; SBS, sensor-based sorting; SI, singled.

* Corresponding author.

E-mail address: nils.kroell@ants.rwth-aachen.de (N. Kroell).

<https://doi.org/10.1016/j.resconrec.2023.106873>

Received 4 November 2022; Received in revised form 9 January 2023; Accepted 10 January 2023

Available online 9 February 2023

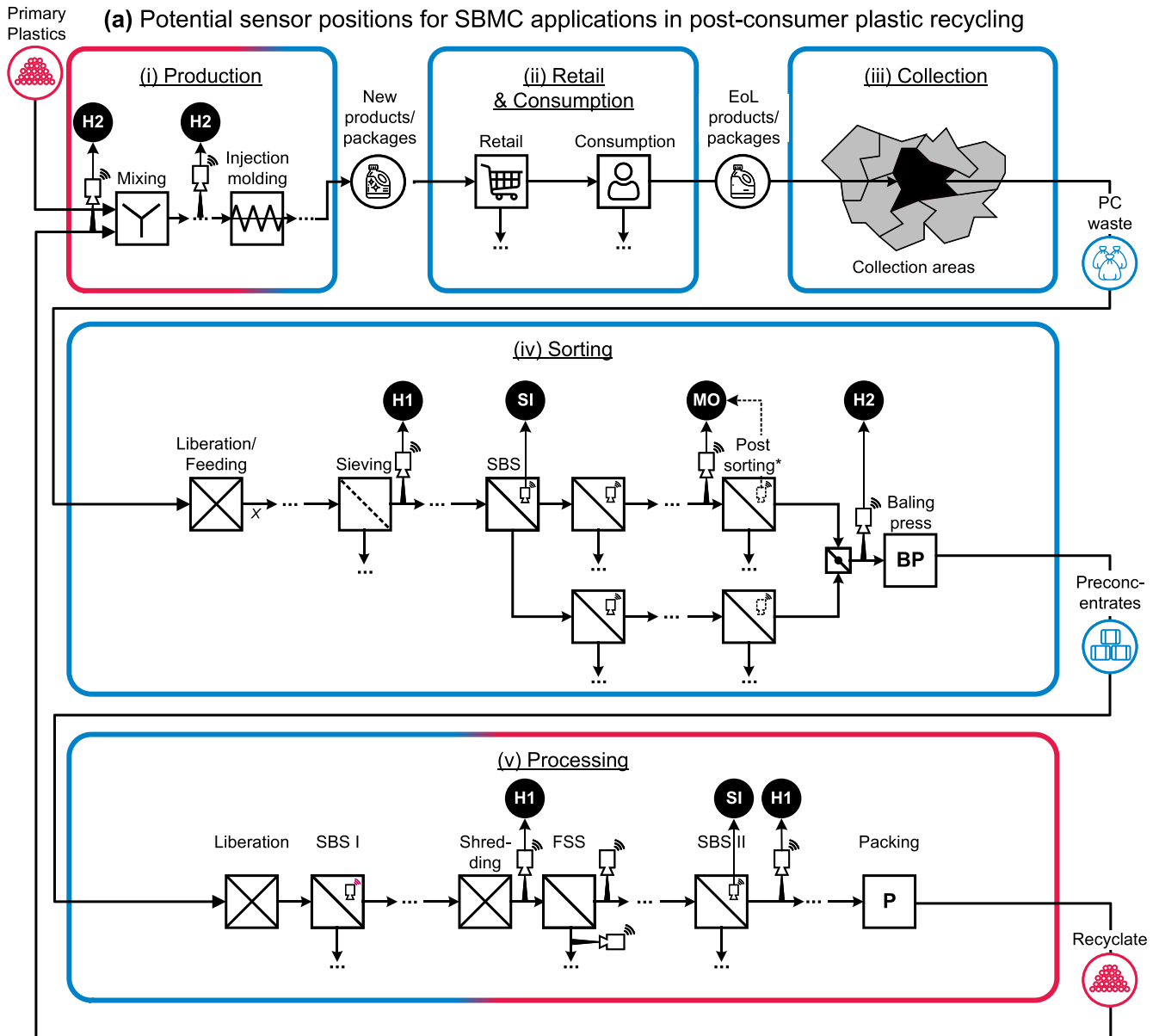
0921-3449/© 2023 The Authors. Published by Elsevier B.V. This is an open access article under the CC BY license (<http://creativecommons.org/licenses/by/4.0/>).

1.1. Mechanical recycling of post-consumer plastics

Mechanical recycling of post-consumer plastics involves three stages: First, end-of-life plastic products and packages are collected according to country-specific collection schemes (e.g., “lightweight packaging waste” [LWP] in Germany or “plastic packaging, metal packaging, drinks cartons” in Belgium). Second, *sorting plants* sort the collected plastic wastes

into material-, polymer-, or color-specific pre-concentrates. Third, specialized *processing plants* purify the pre-concentrates into plastic recyclates. These recyclates can then substitute primary plastics and achieve environmental benefits as outlined above. (Feil and Pretz, 2020)

However, taking the EU27+3 countries as an example, only 8.5 wt% of the plastic demand in 2020 could be covered by post-consumer recyclates due to high material losses along the value chain (Plastic



(b) Resulting material flow presentations

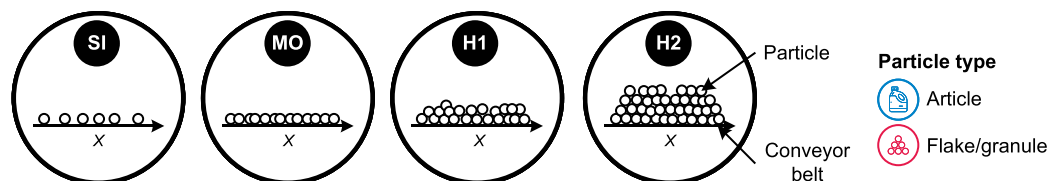


Fig. 1. Potential applications of novel SBMC methods in consumer-based plastic cycles and resulting material flow presentations. (a) Simplified overview of consumer-based plastic cycles with selected, potential sensor positions; (b) simplified cross-section view of different material flow presentations: singled (SI), monolayer (MO), multilayered bulk with bulk heights H1 and H2. x: conveying direction, BP: bale press, P: Packing, FSS: float sink separation, PC: post-consumer; *post sorting can be performed automatically with sorting robots, manually, or not at all; in the case of post sorting through sorting robots, the resulting data streams may also be available for material flow characterization.

Europe, 2022): From 29.5 Mt/a collected post-consumer plastics in the EU27+3, only 34.6 wt% (10.2 Mt/a) (Plastic Europe, 2022) were sent as plastic pre-concentrates to processing plants. Of the 9.1 Mt/a plastic pre-concentrates treated in EU27+3 processing plants, only 60.4 wt% (5.5 Mt/a) (Plastic Europe, 2022) resulted in plastic recyclates. In addition, low and/or unknown plastic recyclate qualities hamper primary plastic substitution in applications with high-quality requirements and the general acceptance of plastic recyclates (Alassali et al., 2021).

1.2. Sensor-based material flow characterization

A promising approach to both minimize material losses and increase product qualities in mechanical plastic recycling lies in novel *sensor-based material flow characterization* (SBMC) applications. In SBMC, sensors and (machine learning) algorithms are used to digitally characterize material flows. Based on material flow characteristics acquired through SBMC, new applications can be envisioned for the optimization of mechanical recycling processes (Fig. 1). (Kroell et al., 2022a)

For SBMC applications in mechanical recycling of post-consumer plastics, *material flow compositions* (MFCOs) are of particular interest (Kroell et al., 2022a). Today, MFCOs in plastic recycling are (almost exclusively) determined through sampling and manual sorting analysis, which is time- and cost-intensive and thus often only conducted on an irregular basis. The resulting intransparency due to the unknown MFCOs results potentially in large inefficiencies. In the future, SBMC methods could help achieve transparency at lower costs and pave the way to new applications that help increase the quality and quantity of recycled plastics:

First, MFCOs inside sorting and processing plants could enable an adaptive and intelligent process control to enhance the plant performance and availability (Fig. 1a.iv and v). For example, SBMC data could enable novel *sensor-based process monitoring* (e.g., Kroell et al., 2022b; Schlögl and Küppers, 2022) or *sensor-based process control* (e.g., Küppers et al., 2022) applications.

Second, information on output MFCOs could make *sensor-based quality control* of product fractions from sorting and processing plants possible (Fig. 1a.iv and v). For example, adaptive pricing models could be implemented based on SBMC data, or sorting products with low quality can be identified for possible reprocessing (Kroell et al., 2022a).

Third, input MFCOs based on SBMC in sorting plants could enable the monitoring and improvement of separate waste collection (Fig. 1a.iii). For example, material losses during waste collection could be reduced by more efficiently allocating and assessing public information campaigns for separate waste collection (Initiative „Mülltrennung wirkt“, 2021).

However, all SBMC applications rise and fall with the *accuracy* (ISO 5725, 2022) of the sensor-based determined MFCOs: If MFCOs cannot be quantified accurately, then (i) adaptive process control algorithms cannot identify optimal machine parameters (Küppers et al., 2022), (ii) confidence in statements of potential sensor-based quality monitoring systems is not given, and (iii) input material flows cannot be reliably monitored.

1.3. Accuracy of sensor-based determined MFCOs

SBMC data processing can be divided into pixel, particle, and material flow levels (Kroell et al., 2022a). At the pixel- and particle-level, several studies have already demonstrated that non-carbon-black standard plastics can be differentiated with > 99% classification accuracy by appropriate classification algorithms due to their unique near-infrared (NIR) spectra (Kroell et al., 2022a). While several SBS manufacturers are already providing area-based material statistics from existing SBS equipment to plant operators (e.g., Binder+Co AG, 2022; Pellenc ST SAS, 2022; REDWAVE, 2022; Sesotec GmbH, 2022; STEINERT GmbH, 2022; TOMRA System ASA, 2022), two critical research gaps remain unsolved:

Research gap 1: Provision of mass-based indicators. Pixel-based classified NIR data provides only *area-based* information on MFCOs, while product qualities and separation processes are assessed using *mass-based* indicators (Kroell et al., 2021; Kroell et al., 2022a). Due to different material densities and grammages, area-based material flows compositions cannot be directly converted into mass-based MFCOs (Kroell et al., 2021). In previous work (Kroell et al., 2021), it was demonstrated that individual particle masses can be predicted from 2D and 3D sensor data using material-specific grammages (mass per area occupied at the conveyor belt) or machine learning models at the particle level. However, the question of how the accuracy of mass predictions contributes to the overall accuracy of MFCO determination at the material flow level remains unsolved.

Research gap 2: Consideration of different material flow presentations. Within sorting and processing plants, material flows are conveyed in different *material flow presentations* (MFPs):

- In sensor-based sorting (SBS) stages, material flows are usually presented as *singled monolayers* on acceleration belts to the SBS units to achieve sufficient sorting results (Feil et al., 2021; Kroell et al., 2022b), i.e., materials do not overlap or touch each other on the conveyor (Fig. 1b.SI).
- For preconditioning processes (e.g., wind-shifting), a MFP as *monolayers* (i.e., particles touch but do not largely overlap each other; Fig. 1b.MO) is often sufficient.
- For material transportation, material flows are often transported as *multilayered bulks* (i.e., particles overlap each other; Fig. 1b.H1/H2) (Kroell et al., 2022a).

Since NIR is a surface measurement technology with a limited penetration depth (Chen et al., 2021b), only the composition of the material flow surface can be determined with NIR, which might differ from that of the full material flow (Kroell et al., 2022a). Thus, it is still unclear (a) if SBMC of post-consumer plastics in the case of missing material singling is technically feasible at all and (b) how accurate the obtained MFCOs are under different MFPs (Kroell et al., 2022a).

1.4. Aim and research question

This study aims to evaluate the technical feasibility and quantify the accuracy of NIR-based MFCO determination of post-consumer plastics. More specifically, we aim to answer the following research question: *How accurate are NIR-based determined MFCOs (i) for different particle types (i.e., flakes and articles, cf. Fig. 1b), (ii) at different material flow presentations, and (iii) based on different data processing techniques?*

2. Material and methods

To answer this research question, we created binary material mixtures of plastic flakes and articles with defined MFCOs. We presented these mixtures at different MFPs (cf. Fig. 1b) to a state-of-the-art NIR sensor, which classifies the material flow pixel by pixel into pre-defined material classes. Subsequently, the number of pixels per material class of a given evaluation area were counted. Different models (density, grammages, and regression) were used to estimate MFCOs from NIR-based pixel counts. Estimated MFCOs were then compared to known MFCOs from creating the mixtures to assess the accuracy of NIR-based MFCO determination.

2.1. Materials and mixtures

Our investigations were structured into two test series: In test series T1, the determination of MFCOs of plastic flakes is investigated to simulate applications in processing plants (cf. Fig. 1a.v). In test series T2, post-consumer plastic packaging articles are studied to simulate applications in sorting plants (cf. Fig. 1a.iv).

2.1.1. Plastic flakes (T1)

To obtain pure plastic flakes, white high-density polyethylene (HDPE) and transparent polyethylene terephthalate (PET) plates of 3 mm thickness from S-POLYTEC GmbH (Goch, Germany) have been subsequently comminuted in rotary shear (see Table S1 in supplementary materials for technical data) for primary comminution and in a cutting mill (Table S2) for secondary comminution. Afterward, the ground plastic flakes have been sieved on a analytical sieve (Table S3) to obtain plastic flakes in the particle size range of 10 mm – 20 mm, which is a common particle size range in plastic processing (Maisel et al., 2020). Fig. 2a-c show exemplary RGB and false-color images as well as projection area distributions of the investigated plastic flakes.

2.1.2. LWP samples (T2)

For T2, HDPE packaging, PET bottles, and beverage cartons (BCs) were sampled from the LWP sorting plant Hündgen Entsorgungs GmbH & Co. KG (Swisttal, Germany). Each material fraction product fraction was sampled from the respective product fraction at the end of the sorting process (1 m³ total sampling volume per product fraction). To ensure maximum representativity during sampling, the full material flow was sampled from a continuously falling material stream according to (Länderarbeitsgemeinschaft Abfall, 2001). The particle size range of the investigated LWP samples is approx. 60 mm – 240 mm (see [Kroell et al., 2021] for further details on the sampling campaign). Afterward, remaining impurities (fines [< 60 mm] and non-target material) were manually removed to obtain pure material fractions of each material (cf. Fig. 2d-f).

2.1.3. Binary mixtures

Three types of binary mixtures were generated to simulate the influence of different materials and particle types: (T1) HDPE and PET flakes, (T2a) post-consumer HDPE and PET packaging, and (T2b) post-consumer HDPE and BC packaging. For all three mixtures, $n = 11$ HDPE shares were investigated: 0%; 0.1%; 0.5%; 1%; 2.5%; 5%; 10%; 20%; 30%; 40%; and 50%.

For T1, raw densities of PET and HDPE flakes are known ($\rho_{V, HDPE} = 0.96$ g/cm³, $\rho_{V, PET} = 1.27$ g/cm³), thus mass-based (w_i) and volume-based MFCOs (φ_i) can be converted into each other using Eq. (1). To eliminate the known density influence on NIR-based determination from Eq. (1) and to make the results easier transferable to mixtures with different density combinations (e.g., polypropylene or polyvinyl chloride), HDPE shares for T1 are prepared in volume percent (φ_i) and we focus on the prediction from area-based (α_i) into volume-based (φ_i) MFCOs within this study.

$$w_i = \frac{\varphi_i \cdot \rho_{V,i}}{\sum_j \varphi_j \cdot \rho_j} \quad (1)$$

For T2 (post-consumer packaging waste), an indication of material densities is not possible due to post-consumer waste characteristics (e.g., post-consumer effects, residual content, material composites, hollow spaces). Thus, material mixtures of T2 were created in wt%.

2.2. Experimental setup

For both test series, the measuring situation in a processing plant (T1) and sorting plant (T2) was simulated using a lab-scale (T1) and technical-lab-scale (T2) test rig to take different particle sizes into account and to enable sufficiently high sample sizes. Each test rig consists of (i) a feeding unit and a conveyor belt to create different MFPs and (ii) a NIR sensor for data acquisition (Fig. 2g).

2.2.1. Material flow presentation

Mixtures were presented in four different MFPs to the NIR sensor to simulate different scenarios defined in Fig. 1b: singled monolayer (SI), monolayer (MO), bulk height h_1 (H1), and bulk height h_2 (H2) ($h_2 > h_1$;

T1: $h_1 \approx 10$ mm, $h_2 \approx 17$ mm; T2: $h_1 \approx 150$ mm, $h_2 \approx 300$ mm). Fig. 2h-k show the belt occupation and bulk heights of the four different MFPs exemplarily for T1 based on 3D laser triangulation recordings.¹

For T1, different MFPs were achieved through a vibrating conveyor operated at different conveying speeds (Fig. 2g.F1). For T2, an ascending conveyor was used for feeding in the SI and MO trials (Fig. 2g.F2) and a dosing bunker with a stamp for the feeding in the H1 and H2 trials (Fig. 2g.F3). In both test series, black conveyor belts were used for material transportation (conveyor width: $b_{T1} = 385$ mm, $b_{T2} = 845$ mm; conveying speed: $v_{T1} = 0.25$ m/s, $v_{T2} = 1$ m/s).

Since the recording of the sensor data was technically limited to 60 s per trial (maximum recording time of uninterrupted false-color data), the material mixtures per trial were adapted to the respective MFP: The feed volumes (V_i) in individual test series and MFPs were $V_{SI} \approx 6$ L, $V_{MO} \approx 10$ L, $V_{H1,H2} \approx 12$ L for T1 and $V_{SI,MO} \approx 300$ L, $V_{H1,H2} \approx 500$ L for T2. Each mixture was measured $n = 10$ (T1) and $n = 5$ (T2) times for each HDPE share and MFP, resulting in a total of $n = 880$ trials.

2.2.2. NIR recording and classification

2.2.2.1. Sensor. In both test series, a Helios-G2–320 NIR sensor from EVK DI Kerschhaggl GmbH (Raaba, Austria) was used to capture and classify the NIR spectra (see [EVK Kerschhaggl GmbH, 2022a] for further details). The used spectral range of the sensor was 990 nm to 1678 nm with a spectral resolution of 3.1 nm/band. The used NIR sensor has an on-chip classification engine, which is frequently used in different industrial and research applications (e.g., Curtis et al., 2021; Friedrich et al., 2022; Kleinhans et al., 2022; Kroell et al., 2022a; Küppers et al., 2022; Schlögl and Küppers, 2022). The resulting spatial resolution of the NIR sensors is 1.08 mm/px and 3.50 mm/px for T1 and T2, respectively². Four halogen lamps with a power of 400 W each were used as emitters (T1: two halogen lamps each from front and back, T2: four halogen from front), and the reflection of radiation from the surface is captured by the NIR sensor. The sensor was calibrated using a white ceramic tile and emitters switch on (white calibration) and the black conveyor belt with emitters switched off (black calibration) as targets using the EVK SQALAR software (EVK Kerschhaggl GmbH, 2022b).

2.2.2.2. Classification model. For each test series, a classification model was developed to classify each spectrum into background (conveyor belt) and user-defined material classes (T1: HDPE, PET; T2: HDPE, PET, BC). For background definition, a threshold was defined to segment the recordings into background and foreground (materials) based on the mean intensity of each spectrum. For material classification, the on-sensor CLASS32 algorithm from EVK DI Kerschhaggl GmbH (Raaba, Austria) was used. In CLASS32, NIR spectra are firstly preprocessed (first derivative, normalization, and smoothing) and then compared to user-defined reference spectra.

For defining NIR reference spectra (cf. Fig. S1 and Fig. S2 in supplementary materials), representative regions of interest were selected for each material class. For T1, spectra were selected from the center of the plastic flakes to avoid edge effects (Chen and Feil, 2019; Küppers et al., 2019a). Accordingly, reference spectra of non-sleeved and non-labeled parts of the LWP samples were selected for T2. Additionally, overlays of transparent materials on top of other materials were added as reference spectra to avoid systematic misclassifications due to mixed NIR spectra in the case of transparency (e.g., a PET bottle on top of a HDPE bottle is classified as PET), cf. (Kleinhans et al., 2022).

¹ See Kroell et al. (2021) for a detailed method description on the used 3D laser triangulation recording.

² Length and width of square pixels after spatial calibration (Section 2.3.1).

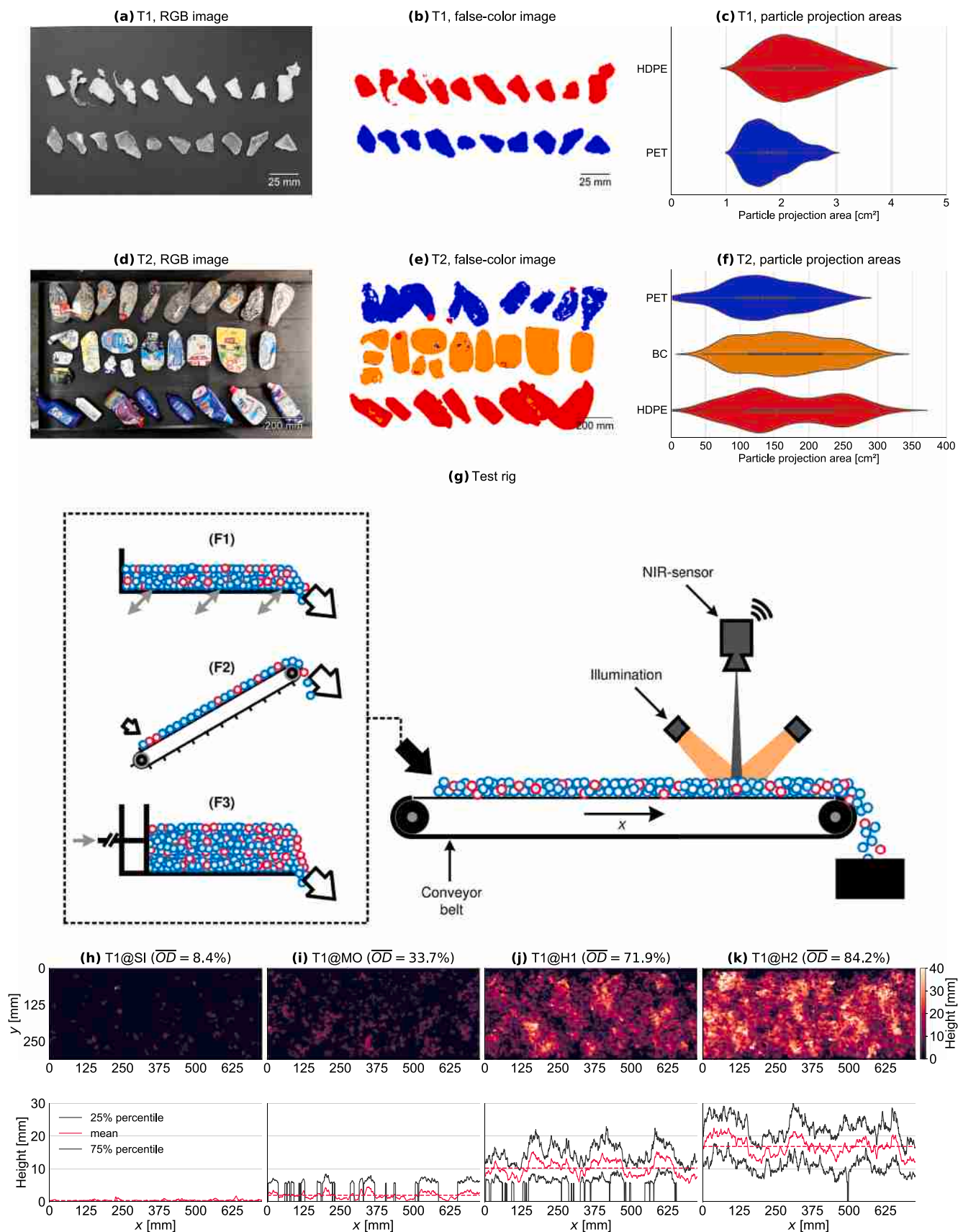


Fig. 2. Materials and methods. (a, d) RGB image, (b, e) resulting NIR false-color image (see [c] and [f] for color legend, respectively), (c, f) distribution of particle projection areas per material for test series T1 (plastic flakes) and T2 (post-consumer plastic packaging), respectively; (g) test rig for T1 and T2; F1: vibrating conveyor, F2: ascending conveyor, F3: dosing bunker with stamp; (h-k) 3DLT recording for different MFPs in T1; \overline{OD} : mean occupation density.

2.3. Data evaluation

For data evaluation, custom Python 3.10 scripts were developed. For data analysis and visualization, primary the open-source packages *Numpy* (Harris et al., 2020) [data storage and data processing], *pandas* (McKinney, 2010; The pandas development team, 2020) [data storage and data processing], *OpenCV* (Bradski, 2000) [pre-processing of false-color images], *scikit-image* (van der Walt et al., 2014) [pre-processing of false-color images], *imea* (Kroell, 2021) [extraction of particle measurements], *scikit-learn* (Pedregosa et al., 2011) [training and evaluation of regression models], *SciPy* (Virtanen et al., 2020) [statistics], *matplotlib* (Hunter, 2007) [data visualization], and *seaborn* (Waskom, 2021) [data visualization] have been applied.

2.3.1. Calibration and data extraction

Each image was firstly calibrated to ensure the same spatial resolution in x- (conveying direction) and y-direction ("square pixels"). Then, row-wise pixel counts are extracted from each image within a region of interest. Due to the batch-wise tests, lower particle throughputs occur at the beginning and the end of each trial, which could distort the results due to lower occupation densities (share of the conveyor belt covered by material) compared to the MFPOs to be simulated. Therefore, an automated method for defining the region of interest has been developed: First, the cumulative distribution of non-background pixels from start until end of each trial is calculated and normalized to 100%. Then, the region of interest is defined as all rows that lie in an interval of $[t_1, t_2]$ of this cumulative distribution. In this study, the selected interval was [20%, 80%], i.e., the middle 60% of the total material area per trial is extracted to eliminate lower, unrepresentative belt occupations at the beginning and the end of each trial.

2.3.2. Data aggregation: chunks and moving averages

To determine time-resolved MFPOs, false-color pixels of a given area must first be aggregated before they can be converted to MFPOs. In the following, we will refer to these aggregation areas as *chunks*.

To quantify the influence of different chunk sizes on SBMC accuracies, a range of different chunk sizes is investigated. For broad applicability of the results, we report the investigated chunk sizes in $[m^2]$ instead of $[s]$ since this allows universal indications independent of specific conveyor belt widths and speeds. For defining the chunk area, we compare two approaches: (i) the projection area of the total conveyor surface incl. material (*conveyor area*, $A_{\text{chunk,conveyor}}$) and (ii) the projection area covered by material (*material area*, $A_{\text{chunk,material}}$). For a given application, the area-based chunk definition ($A_{\text{chunk,conveyor}}$ or $A_{\text{chunk,material}}$) can be converted to a time-based chunk definition based on the known belt speed v , conveyor width b , and occupation density OD using Eq. (2):

$$\Delta t_{\text{chunk}} = \frac{A_{\text{chunk,conveyor}}}{v \cdot b} = \frac{A_{\text{chunk,material}}}{OD \cdot v \cdot b} \quad (2)$$

For example, a material-area-based chunk size of $A_{\text{chunk,material}} = 1 \text{ m}^2$ on a sensor-based sorter with the parameters $v = 3 \text{ m/s}$, $b = 2 \text{ m}$ and $OD = 20\%$ equals a time-based chunk size of $\Delta t_{\text{chunk}} = 0.83 \text{ s}$.

2.3.3. Pixel-to-MFPO-models

While pixel-based NIR classification describes material flows in terms of areas, mass-based MFPOs are needed in most SBMC applications (cf. research gap 1, Section 1.3). Therefore, we differentiate between three types of MFPOs within this study: The *mass share* w_i (Eq. (3)) (DIN 1310, 1984), the *volume share* φ_i (Eq. (4)) (DIN 1310, 1984), and the *area share* α_i (Eq. (5)). Where m_i , V_i , and A_i are the mass, volume, and projection area (as recorded by the NIR sensor) of fraction i , and m , V , and A are the total masses, volumes, and projections areas, respectively.

$$w_i = \frac{m_i}{m} \quad (3)$$

$$\varphi_i = \frac{V_i}{V} \quad (4)$$

$$\alpha_i = \frac{A_i}{A} \quad (5)$$

As elaborated in Section 2.1.3, material mixtures for T1 are given in HDPE volume shares (φ_{HDPE}) and we will determine how accurately these can be predicted from the area-based HDPE shares (α_{HDPE}) from the NIR false-color data. In the following, we will refer to this model as the *density model*.

For T2, two pixel-to-MFPO models are compared. First, we apply material-specific grammages (Eq. (6)) to transform the area-based HDPE shares (α_{HDPE}) into estimated mass-based HDPE shares (\hat{w}_{HDPE}) according to Kroell et al. (2021) by using Eq. (7) (*grammage model*). The determined grammages for T2 in this study are $\rho_{A, \text{HDPE}} = 2.38 \text{ kg/m}^2$, $\rho_{A, \text{PET}} = 2.19 \text{ kg/m}^2$, and $\rho_{A, \text{BC}} = 1.49 \text{ kg/m}^2$.

$$\rho_{A,i} = \frac{m_i}{A_i} \quad (6)$$

$$w_i = \frac{\alpha_i \cdot \rho_{A,i}}{\sum_j \alpha_j \cdot \rho_{A,j}} \quad (7)$$

Second, we apply a *regression model* to convert area-based (α_{HDPE}) into mass-based HDPE shares (\hat{w}_{HDPE}). Therefore, we split the NIR data into 70% training and 30% test data. The regression model is then trained on the training data and its prediction accuracy is assessed based on the test data. To avoid overfitting due to the limited investigated HDPE share range (0%–50%, cf. Section 2.1.3), a polynomial regression model (cf. Fahrmeir et al., 2013) with a polynomial degree of two is chosen to investigate a first technical feasibility^{3,4}.

2.3.4. Accuracy assessment

A variety of different metrics exist to assess the accuracy of measurements (ISO 5725, 2022). To translate the intuition of many practitioners regarding the accuracy of SBMC methods into a single metric, we propose the *95% measurement uncertainty* (MU_{95}). The MU_{95} is the 95th percentile (P_{95}) of all absolute errors between a set of measurands X_{measured} and its corresponding true values X_{true} (Eq. (8)).

$$MU_{95} = P_{95}(|X_{\text{measured}} - X_{\text{true}}|)$$

$$\text{with } X = \{x_1, \dots, x_n\} \quad (8)$$

The MU_{95} for a set of measurements indicates that in 95% of all cases in the measurements, the true MFPO (x_{true}) is in the range $x_{\text{measured}} \pm MU_{95}$. For example, if a plant operator is using an inline-NIR material flow monitoring system with a MU_{95} of 5 wt% and the NIR system is displaying a value of $x_{\text{measured}} = 50 \text{ wt\%}$, the true MFPO is between 45 wt% and 55 wt% in 95 of 100 measurements. The motivation behind using a 95% percentile instead of, e.g., maximum errors is to exclude potential outliers and thus to account for the often high heterogeneity of anthropogenic material flows. In addition to the proposed MU_{95} metric, results are reported as mean absolute errors (*MAE*) and R^2 -scores to provide better comparability for readers used to *MAE* and R^2 metrics. Accurate measurements are characterized by low MU_{95} and *MAE* values and R^2 -scores close to 100%.

³ Note that the presented approach can be easily extended to more complex regression models (e.g., neural networks), if wider ranges of training data is available.

⁴ The motivation behind using a polynomial regression model of the second degree is that (a) the relation between area-based and mass-based MFPOs is non-linear (cf. Eq. (7)). A linear regression would result in *underfitting*, while (b) higher polynomial degrees would result in *overfitting* due to limited training data (0%–50% HDPE share).

3. Results and discussion

The following sections aim at answering the research question raised in Section 1.4 regarding the influence of different particle types (Section 3.1), MFPs (Section 3.2), and data processing techniques (Section 3.3).

3.1. Influence of particle types

3.1.1. Classifiability

As evident from Fig. 2b and Fig. 3a-b, the trained classification model for T1 can differentiate HDPE, PET and background very accurately. The classification model for T2 also succeeds in providing a satisfactory distinction between HDPE, PET, BC, and background (Fig. 2e; Fig. 3c,e). However, the overall classification accuracy is lower, likely due to three major effects:

- (1) Thin-walled areas of PET bottles are sometimes falsely classified as background (Fig. 2e, Fig. 3c). Due to their transparency, most of the radiation is transmitted through the PET bottles and absorbed by the black conveyor belt. Thus, only a small proportion of the radiation is reflected and captured by the NIR sensor (cf. Küppers et al., 2019b).
- (2) Combinations of sleeves or labels and packaging material result in mixed NIR spectra, which can influence the classification result (Chen et al., 2023; Küppers et al., 2019a; Schlögl and Küppers, 2022). For example, a paper label on top of a HDPE canister has mixed NIR spectra of paper and HDPE, which is similar to the NIR spectra of BC (made from a HDPE inlay and paper fibers); thus, some paper labels are classified falsely as BC (Fig. 2e, Fig. 3c,e).
- (3) We observe some misclassifications from dark parts of BCs as PET (Fig. 2e, Fig. 3e), which might be caused by the lower NIR reflectance due to the dark color or by a direct reflectance of shiny BC parts.

3.1.2. Correlation between NIR-based and true MFCOs

3.1.2.1. Plastic flakes (T1). Fig. 3b compares the pixel-based HDPE shares obtained through the NIR classification (α_{HDPE}) with the true volume-based HDPE share (φ_{HDPE}) obtained when creating the material mixtures. Overall, the pixel-based and true HDPE shares correlate strongly with a Pearson correlation coefficient (Pearson, 1895) of $PCC_{T1} = 99.5\%$.

However, with increasing true HDPE share, the area-based HDPE share from the NIR sensor increasingly overestimates the corresponding true HDPE share ($p < 0.001$)⁵. A likely reason for this overestimation could be the different surface-area-to-volume ratios of the investigated HDPE and PET flakes, which can be traced back to the different comminution behavior of both polymers: Since HDPE is softer, more fraying of HDPE occurred during shredding compared to PET (cf. Fig. 2a), resulting in an increased projection area of HDPE compared to PET (HDPE flakes: $718 \text{ m}^2/\text{m}^3$, PET flakes: $476 \text{ m}^2/\text{m}^3$). As a result, the area-based HDPE share is overestimated by $+4.90 \text{ vol}\%$ at $\varphi_{\text{HDPE}} = 50 \text{ vol}\%$.

3.1.2.2. Plastic packaging articles (T2). Fig. 3d and Fig. 3f compare the predicted mass-based HDPE shares based on NIR data using the grammage model (\hat{w}_{HDPE} , cf. Section 2.3.3) with the true mass-based HDPE shares (w_{HDPE}). For T2, predicted and true HDPE-shares correlate strongly with each other ($PCC_{T2a} = 98.8\%$, $PCC_{T2b} = 96.4\%$), but slightly lower than T1.

Similar to T1, the NIR-based characterization overestimates the true

HDPE share for T2a and T2b, but because of different reasons. While the samples shown far left in Fig. 3c-e represent pure PET and BC fractions ($w_{\text{HDPE}} = 0\%$) in article-based manual sorting analysis, the pixel-based NIR characterization identifies HDPE shares of $5.4 \text{ a}\%$ ($5.9 \text{ wt}\%$) and $2.0 \text{ a}\%$ ($3.2 \text{ wt}\%$) for T2a and T2b, respectively. Reason for this difference is the different counting basis of both methods: While HDPE caps, e.g., on PET bottles, count as “PET” in manual analysis, they are (correctly) classified and counted as “HDPE” in the pixel-by-pixel NIR characterization.

The HDPE-overestimation decreases with higher true HDPE share, as the material flow contains more “true” HDPE from HDPE packaging and fewer “false” HDPE caps from PET bottles. Additionally, labels on true HDPE packaging classified as BC reduce the predicted HDPE share and simultaneously increase the predicted share of other material classes (e.g., paper-based labels on HDPE containers that are classified as BC).

3.2. Influence of material flow presentation

3.2.1. Plastic flakes (T1)

HDPE-overestimation in T1 differs significantly between different MFPs (mean over all trials: SI: $+2.63\%$, MO: $+0.92\%$, H1: $+0.08\%$, H2: $+0.32\%$), see Fig. 3b. Quantitatively, we can show that the HDPE-overestimation decreases with increasing occupancy density ($p = 0.04$).

A possible reason for this effect could be the lower thickness of frays compared to the main part of the flakes: If a HDPE fray overlays the black conveyor belt, it is usually classified either as HDPE or as background (depending on material thickness and background definition in the NIR classification; cf. Fig. 2b). At higher occupation densities, HDPE flakes lie on top of other flakes. If a HDPE fray is on top of another HDPE flake, it is usually classified as HDPE, but if a HDPE fray overlays a PET flake, a mixed HDPE/PET spectra can occur due to the penetration depth of NIR (Chen et al., 2021b, 2023). Since mixed PET/HDPE spectra from transparent PET on top of HDPE are trained as “PET” to the classification model⁶ (cf. Section 2.2.2.2), the HDPE frays on top of PET might be classified as PET in some cases, resulting in a lower HDPE-overestimation at higher occupation densities.

3.2.2. Plastic packaging articles (T2)

No significant differences are observed when comparing the predicted MFCOs of SI vs. MO as well as H1 vs. H2. In contrast, the predicted MFCOs differ significantly between non-overlapping (SI, MO) and overlapping (H1, H2) MFPs, which might be explained by the following two mechanisms.

3.2.2.1. Classification behavior at different MFPs. For T2a, HDPE-overestimation of pure fractions ($w_{\text{HDPE}} = 0\%$) is significantly ($p < 0.001$) higher for non-overlapping (SI: $+5.87 \text{ wt}\%$, MO: $+5.84 \text{ wt}\%$) compared to overlapping MFPs (H1: $+3.61 \text{ wt}\%$, H2: $+3.60 \text{ wt}\%$). A possible explanation for this is the better detectability of thin-walled PET bottles on top of other materials in comparison to the black conveyor belt: Two thin-walled PET bottles on top of each other have a higher overall material thickness, which results in a higher mean intensity of the reflected NIR spectra that is usually more often classified as PET instead of background. A thin-walled PET bottle on top of HDPE packaging results in mixed PET/HDPE spectra, which are trained as PET to the classification model (cf. Section 2.2.2.2). Thus, less PET is recognized at non-overlapping MFPs, which results in higher predicted HDPE shares compared to overlapping MFPs.

For T2b, the HDPE-overestimation is higher at overlapping vs. non-overlapping MFPs (e.g., at $w_{\text{HDPE}} = 0\%$: H1: $+4.47 \text{ wt}\%$, H2: $+4.37$

⁵ p -values express the level of significance: differences are considered statistically significant if the p -value is lower than 0.05.

⁶ HDPE on top of PET is trained as “HDPE”, but the PET influence on a PET+HDPE spectra is lower than the PET influence on HDPE+PET due to the opaque color of HDPE flakes compared to transparent color of PET in this study (cf. Section 2.1.1).

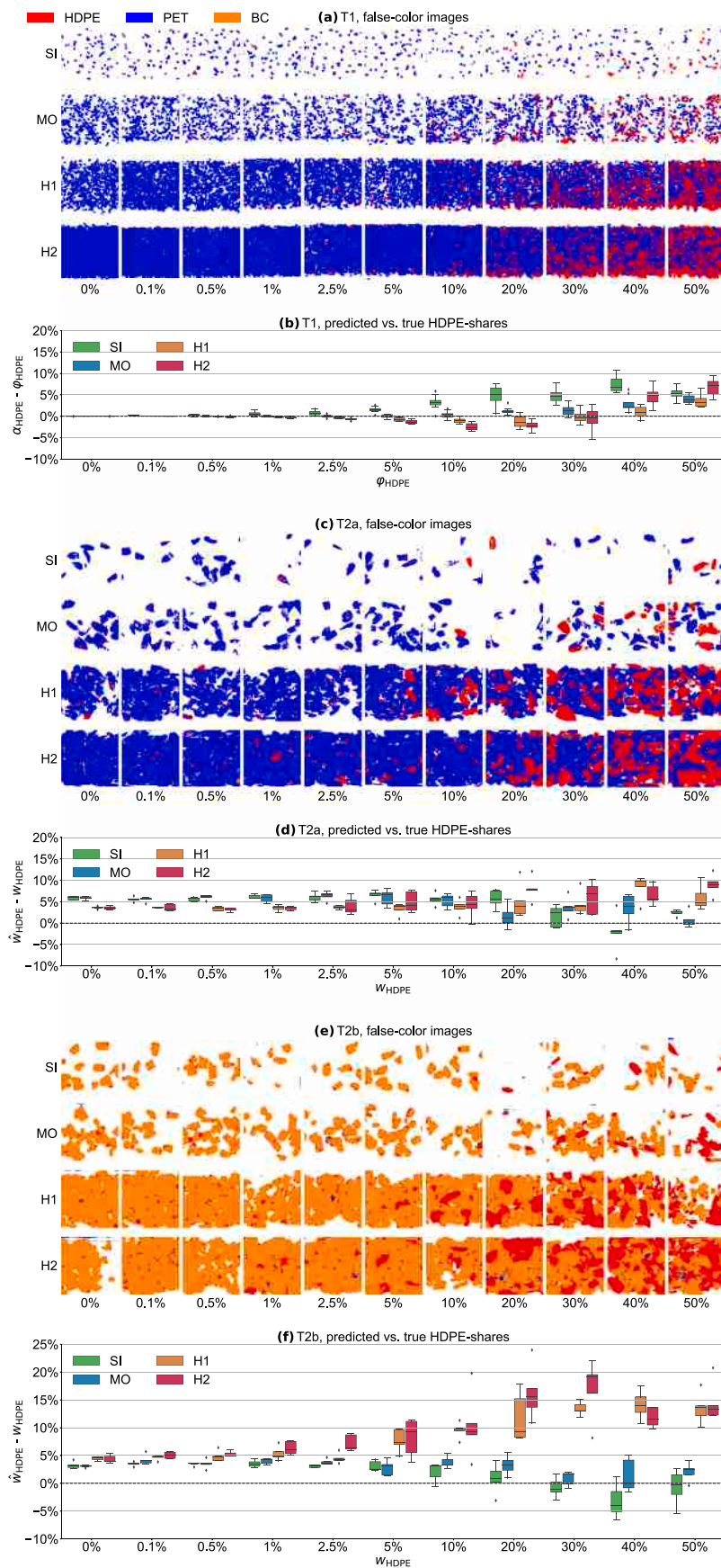


Fig. 3. Influence of particle types and MFP on trial-based prediction errors. (a, c, e) randomly selected quadratic sections of false color images per MFP and true HDPE share; (b, d, f) comparison between predicted and true HDPE share per trial for T1, T2a, and T2b, respectively.

wt% vs. SI: +3.24 wt%, MO: +3.09 wt%). The causes of this behavior cannot be reliably assessed on the data basis of this study. A possible hypothesis for this effect could be different particle orientations, which could result in more HDPE caps facing toward the NIR sensor at overlapping MFPs. However, further research is needed to clarify the mechanisms behind these observations.

3.2.2.2. Segregation effects. In both test series, HDPE shares are disproportionately overestimated with increasing HDPE share: For T2a, the difference between overlapping vs. non-overlapping MFPs ($w_{\text{HDPE, (H1,H2)}} - w_{\text{HDPE, (SI,MO)}}$) increases from -2.2 wt% ($w_{\text{HDPE}} = 0\%$) to +5.8 wt% ($w_{\text{HDPE}} = 50\%$); for T2b, HDPE-overestimation increases from +1.3% ($w_{\text{HDPE}} = 0\%$) to +13.3% ($w_{\text{HDPE}} = 50\%$), cf. Fig. 3d,f.

A possible reason for the accumulation of HDPE articles on the captured material flow surface could be higher particle volumes and three-dimensional shapes of HDPE packaging compared to smaller and/or flattened PET bottles and BCs. Due to the *brazil nut effect* (Rosato et al., 1987), larger HDPE packaging could have accumulated on the material flow surface. Since NIR is a surface measurement method, accumulation of larger articles on the material flow surface will lead to an overestimation of the corresponding material fraction compared to the true MFCO.

3.3. Influence of data processing techniques

This section investigates two data processing techniques to increase the accuracy of NIR-based determined MFCOs: Appropriate *chunk sizes* (Section 3.3.1) aim at reducing random measurement errors (i.e., increasing precision [ISO 5725, 2022]), e.g., due to different particle orientations or particle artifacts. *Pixel-to-MFCO-models* (Section 3.3.2) aim at reducing systematic measurement errors (i.e., increasing trueness [ISO 5725, 2022]), e.g., due to different counting basis of composite materials (cf. Section 3.1) or segregation errors (cf. Section 3.2).⁷

3.3.1. Chunk sizes

Fig. 4 shows the influence of chunk sizes on prediction accuracies (quantified by the MU_{95} metric) and the resulting MFCO time series. As shown in Fig. 4a-l, MUs decrease continuously with increasing chunk size and asymptotically approach a plateau, which represents the systematic differences between NIR-based and manual material flow characterization known from Fig. 3.

3.3.1.1. Definition of reduction ratios. From Fig. 4a-l, we observe a trade-off between low chunk size and low MU: Smaller chunks enable a lower latency between data acquisition and delivery of chunk-based information and higher temporal data resolution. Larger chunks, however, can smooth out unwanted fluctuations and reduce data noise.

To quantitatively describe different weightings between MU and chunk size, we define *reduction ratios* (RR, Eq. (9)) that describe the relative reduction of MU from raw false-color data ($MU_{95,\text{max}}$) towards the MU plateau ($MU_{95,\text{min}}$):

$$RR = \frac{MU_{95,\text{max}} - MU_{95,i}}{MU_{95,\text{max}} - MU_{95,\text{min}}} \quad (9)$$

Based on the reduction ratios, we define three RR scenarios (80%, 95%, and 99% RR) that describe three different weighing between MU and chunk size (from a focus on small chunk sizes [$RR = 80\%$] to focus on low MUs [$RR = 99\%$]).

⁷ To avoid an overrepresentation of the HDPE shares between 0% - 10% (due to the trials at 0.1%, 0.5%, 1%, 2.5%, 5% HDPE share), the ground truth data in Section 3.3 is limited to 0%, 10%, 20%, 30%, 40%, and 50% true HDPE share to achieve an equidistant distribution.

3.3.1.2. Influence of particle types and sizes. As shown in Fig. 4a-l, MU decrease significantly faster for T1 (99% RR at 3.14 m² [mean over all T1 trials]) compared to T2a (13.32 m²) and T2b (16.88 m²). Two possible reasons for the faster decrease of T1 compared to T2 could be (i) higher homogeneity of plastic flakes from T1 compared to plastic packaging articles in T2 (e.g., due to composite packaging, a higher variety of particle sizes and shapes, and post-consumer effects [cf. Fig. 2a,d]) as well as (ii) larger particle sizes in T2 compared to T1 (cf. Fig. 2c,f), which might require larger chunk sizes for smoothing.

3.3.1.3. Influence of MFPs and chunk size definition. As shown in Fig. 4a,e,i, MUs for SI and MO decrease slower and later compared to H1 and H2, when a conveyor-area-based chunk size definition is used (cf. Section 2.3.2). A likely explanation for this observation are different occupation densities for different MFPs: While 1 m² conveyor area for T1 at SI contains on average 0.08 m² material, 1 m² conveyor area at MO, H1, and H2 contain 0.34 m², 0.72 m², and 0.84 m² material, respectively (cf. Fig. 2h-k). Thus, a higher amount of material is aggregated in a chunk at higher occupation densities, which results in stronger smoothing.

In contrast, when a material-area-based chunk size definition is used, MUs decrease almost simultaneously and at a similar pace for different MFPs (Fig. 4b,f,j). The resulting curve trajectories are thus more generalizable and could be used, e.g., to derive chunk sizes in specific SBMC applications.

3.3.1.4. Influence of target material share. Similar chunk sizes are needed to achieve the same RRs across different HDPE shares (cf. Fig. 4c, d,g,h,k,l) and no statistically significant correlation between HDPE share and chunk size at different RRs is found (conveyor-area-based chunk size: $\bar{p} = 0.544$, material-area-based chunk size: $\bar{p} = 0.668$ [mean p -value across all test series and RRs]).

3.3.1.5. Influence of chunk sizes on the resulting MFCO time series. Fig. 4m-x shows the influence of applying different chunk sizes to an exemplary time series (50% HDPE true share) across different MFPs and test series. For all test series, a decreased deviation of the raw sensor data from SI, over MO, H1 to H2 is observed (mean standard deviation of raw sensor data over all test series and HDPE shares: SI: 20.9%, MO: 16.2%, H1: 9.8%, H2: 8.7%). While finer details such as small fluctuations in the HDPE share are still present at 80% RR, these are smoothed out at 95% and 99% RR (cf. Fig. 4m-p).

3.3.2. Pixel-to-MFCO-models

As we have shown in Section 3.1 and Section 3.2, systematic effects such as different area-to-volume ratios, composite effects, and segregation errors lead to less accurate MFCO predictions. This raises the question if information about these effects can be used to correct them and make the MFCO predictions more accurate.

To answer this question, Fig. 5 shows the ground truth data and compares the prediction curves of the investigated models (T1: density and regression model, T2: grammage and regression model): True HDPE shares and pixel-based shares are shown on the x - and y -axis, respectively, and boxplots indicate the distribution of the raw data after applying a moving average (99% RR). Prediction accuracies of both models at different MFPs are quantified in Table 1 using the MU_{95} , MAE, R^2 metric (cf. Section 2.3.4).

In all cases, the regression model outperforms the density/grammage models. For T1 (Fig. 5a), the density model achieves a mean MU_{95} of 5.6 vol% over all MFPs due to the HDPE-overestimation (frays) discussed in Section 3.1.2.1 and Section 3.2.1. In contrast, the polynomial regression model successfully compensates higher area-based HDPE shares and reduces the MU_{95} by a factor of 4.6 down to 1.2 vol%.

For T2a (Fig. 5b), the grammage model results in similar predictions as a naïve prediction would predict ($\hat{w}_i = \alpha_i$), due to similar grammage

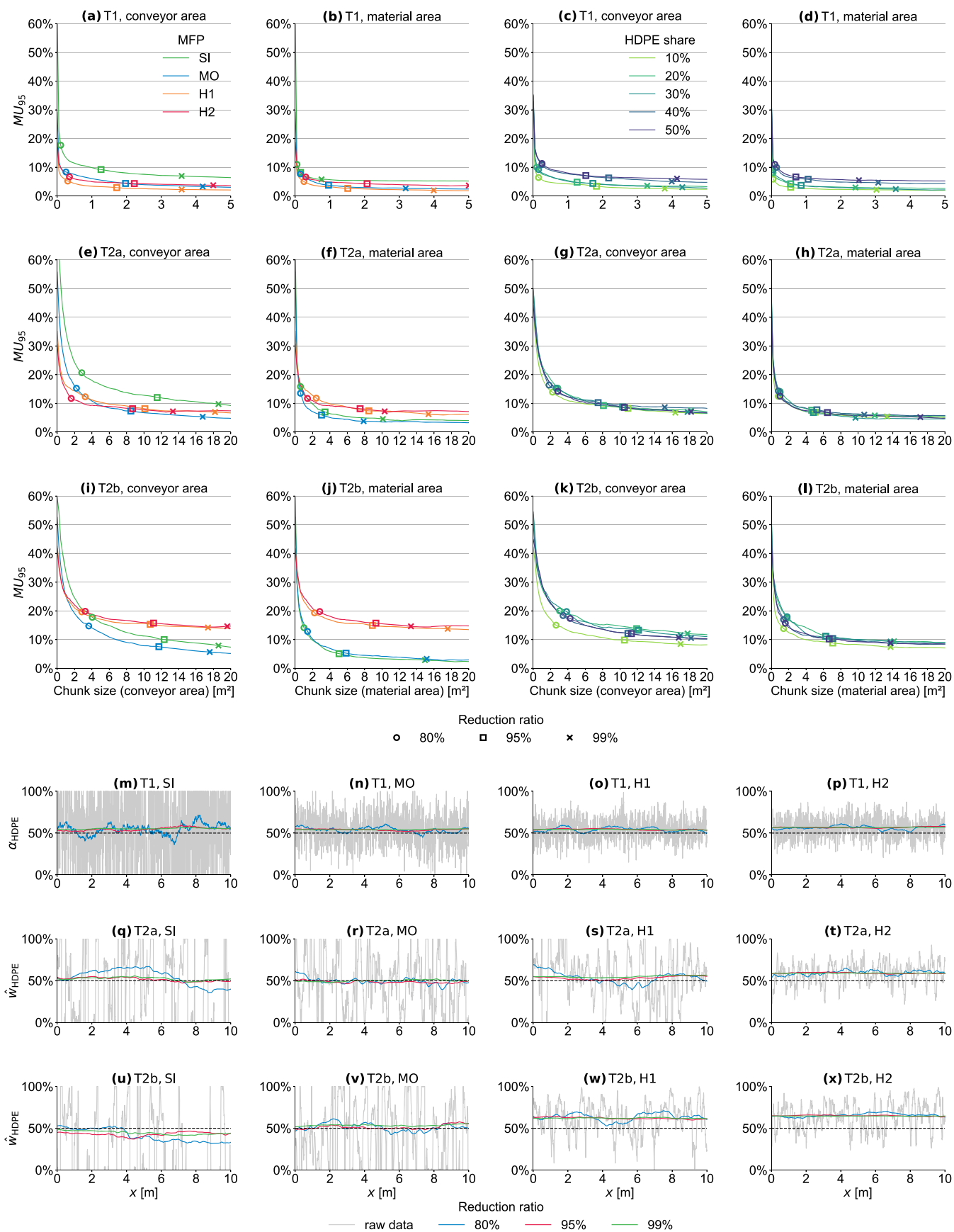


Fig. 4. Influence of chunk size and chunk definition on measurement uncertainty (MU). (a-l) influence of chunk size on MU for different test series, MFPs, and HDPE shares. (m-x) effect of exemplary chunk sizes (80%, 95%, and 99% reduction ratio) on exemplary time series (predicted HDPE share over time) on the example of 50% true HDPE share; T1: percentages in vol%, T2: percentages in wt%.

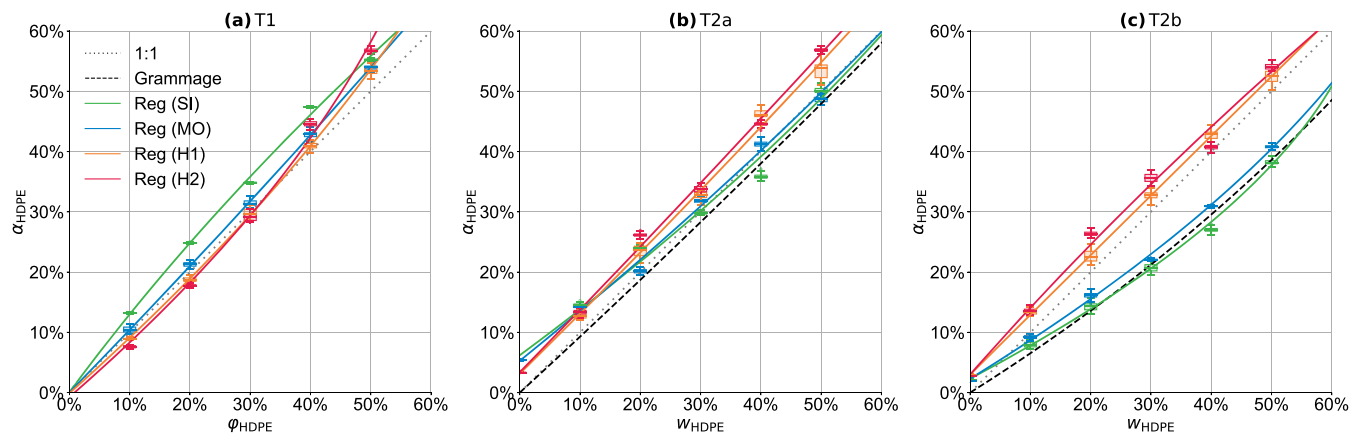


Fig. 5. Comparison of different pixel-to-MFCO-models at 99% reduction ratio (material-based chunk sizes: T1: 3.14 m², T2a: 13.32 m², T2b: 16.88 m²).

Table 1

Accuracy of investigated pixel-to-MFCO-models at 99% reduction ratio (material-based chunk sizes: T1: 3.14 m², T2a: 13.32 m², T2b: 16.88 m²); highest accuracies per test series are highlighted in bold.

Metric	Test series	Model	SI	MO	H1	H2	mean
<i>MU</i> ₉₅	T1	Density	7.4%	4.1%	4.0%	7.0%	<u>5.6%</u>
		Regression	1.3%	0.8%	1.0%	1.8%	<u>1.2%</u>
	T2a	Grammage	5.9%	5.9%	8.6%	9.2%	<u>7.4%</u>
		Regression	3.9%	2.5%	2.7%	2.0%	<u>2.8%</u>
	T2b	Grammage	3.4%	4.2%	14.7%	17.3%	<u>9.9%</u>
		Regression	1.9%	1.3%	1.5%	3.7%	<u>2.1%</u>
<i>MAE</i>	T1	Density	4.2%	1.7%	1.2%	2.8%	<u>2.5%</u>
		Regression	0.5%	0.3%	0.3%	0.8%	<u>0.5%</u>
	T2a	Grammage	3.9%	3.8%	5.2%	6.2%	<u>4.8%</u>
		Regression	1.7%	1.0%	0.9%	0.8%	<u>1.1%</u>
	T2b	Grammage	1.8%	2.5%	11.3%	12.3%	<u>7.0%</u>
		Regression	0.8%	0.7%	0.6%	1.3%	<u>0.8%</u>
<i>R</i> ²	T1	Density	93.7%	98.5%	99.2%	96.7%	<u>97.0%</u>
		Regression	99.8%	99.9%	99.9%	99.7%	<u>99.9%</u>
	T2a	Grammage	91.3%	92.5%	91.8%	88.1%	<u>90.9%</u>
		Regression	98.5%	99.4%	99.5%	99.6%	<u>99.3%</u>
	T2b	Grammage	97.9%	97.2%	64.7%	58.0%	<u>79.5%</u>
		Regression	99.7%	99.8%	99.8%	98.9%	<u>99.5%</u>

of HDPE and PET (caused partially by a lower PET recognition compared to HDPE) (cf. Section 3.1.1). For T2b (Fig. 5c), the grammage model corrects the different grammages of HDPE and BC and is thus closer to the SI and MO data. As a consequence, the grammage model predictions are further away from the H1 and H2 data since the segregation errors are not included. In contrast, the regression model fits the training data of both test series and successfully corrects, e.g., HDPE-overestimations due to segregation errors at H1 and H2 or compound effects (HDPE caps) downward (Fig. 5c). On average, MUs are reduced by a factor of 3.5 ($MU_{95, grammage} = 8.6 \text{ wt\%} \rightarrow MU_{95, regression} = 2.4 \text{ wt\%}$).

The final prediction results when combining sufficiently high chunk sizes (cf. Section 3.3.1) with the polynomial regression model of degree two show that NIR-based MFCOs determination for plastic flakes and LWP packaging is technically feasible. For plastic flakes (T1), mean *MU*₉₅ values of 1.2 vol% (*MAE*: 0.5 vol%, *R*²: 99.9%) are achieved, for post-consumer plastic packaging (T2), mean *MU*₉₅ values were located at 2.4 wt% (*MAE*: 1.0 wt%, *R*²: 99.4%).

4. Conclusion and outlook

SBMC methods promise to significantly improve post-consumer plastic recycling by enabling new applications of sensor technology such as adaptive process control or sensor-based quality control (Kroell et al., 2022a). Fulfilling these promises, however, is only feasible if the generated SBMC data is accurate enough.

While numerous studies have demonstrated high accuracy of NIR-

based plastics classification at the pixel and particle level, it has been unclear what accuracies can be achieved at the material flow level. This study assessed the accuracy of NIR-based MFCO determinations based on three binary mixtures (T1: HDPE and PET plastic flakes, T2a: post-consumer HDPE packaging and PET bottles, T2b: post-consumer HDPE packaging and BCs) and investigated the effects of particle types, MFPs, and data processing techniques on the achievable accuracy.

User-defined settings in the NIR classification model have a large impact on NIR-based MFCO predictions of both **particle types**. Predicted MFCOs are especially influenced by (i) the discrimination between background and (transparent) materials and (ii) the classification of mixed NIR spectra (e.g., labels and sleeves for plastic packaging). For plastic flakes (T1), different surface area-to-volume ratios can result in significant over- and underestimations of the true material share, if area-based NIR classifications are used to determine volume- or mass-based MFCOs. For post-consumer plastic packaging (T2), prediction errors result mainly from the different counting basis of article-based manual sorting and pixel-based NIR characterization. For instance, it was determined that pure PET bottle (T2a) and BC (T2b) fractions from LWP contain approx. 5.4 a% and 2.1 a% HDPE, e.g., due to HDPE bottle caps, respectively.

Concerning the **material flow presentation**, it is important to distinguish between non-overlapping (SI, MO) and overlapping MFPs (H1, H2). On the one hand, material overlays influence the NIR classification behavior in that transparent materials are better detected. On the other hand, segregation errors were detected which led to an

overrepresentation of larger HDPE plastic packaging compared to smaller PET bottles and BCs on the material flow surface captured by the NIR sensor (brazil nut effect). For instance, HDPE contents were overestimated by an additional +5.8 wt% (T2a) and +13.3 wt% (T2b) for overlapping (H1, H2) compared to non-overlapping MFPS (SI, MO) at $w_{HDPE} = 50$ wt%.

Adequate **data processing** can significantly correct the effects presented above and thus increase the accuracy of NIR-based MFCOs: *Random errors* (e.g., due to different particle orientations) can be compensated by aggregating the data over sufficiently large *chunk sizes*. The influence of chunk sizes on measurement accuracies can be described by the material area per chunk: with increasing chunk size, the MU decreases asymptotically. *Systematic errors*, such as composite effects of plastic packaging and segregation errors, can be compensated through regression models. By using a polynomial regression model (polynomial degree two), the MU was on average reduced by a factor of 4.6 and 3.5 compared to density- or grammage-based conversion approaches for T1 and T2, respectively. By combining all findings, accuracies of $MU_{95} = 1.2$ vol% ($MAE = 0.5$ vol%; $R^2 = 99.9\%$) for plastic flakes (T1) and $MU_{95} = 2.4$ wt% ($MAE = 1.0$ wt%; $R^2 = 99.4\%$) for plastic packaging (T2) could be achieved.

Our results show that NIR-based determination of mass-based MFCOs in mechanical recycling of post-consumer plastics is technically feasible. However, they also indicate how significantly external factors like particle characteristics and MFPS can influence measurement accuracy and thus highlight the importance of material- and application-specific data processing techniques.

In future research, our results should be further scaled up. In addition to plant-scale investigations, we consider investigations on non-binary LWP mixtures; transfer to other polymers, particle size distributions, and material flows; as well as gaining a better understanding of segregation processes of anthropogenic material systems like LWP to be of particular importance.

Combining inline NIR sensors and adequate data processing techniques provides meaningful material information not only at the pixel and particle level but also at the material flow level and beyond. Based on the technical feasibility demonstrated in this study, new SBMC applications can be developed to accelerate the transition to more sustainable and efficient post-consumer plastics loops.

Funding

This work was funded by the German Federal Ministry of Education and Research (BMBF) within the program "Resource-efficient circular economy - plastics recycling technologies (KuRT)" under the project *ReVise* (grant no. 033R341) and the National Austrian Research Promotion Agency (FFG) within the program "Production of the Future" under the project *EsKorte* (grant no. 877341). The responsibility for the content of this publication lies with the authors.

CRedit authorship contribution statement

Nils Kroell: Conceptualization, Methodology, Software, Validation, Formal analysis, Investigation, Data curation, Writing – original draft, Writing – review & editing, Visualization, Supervision, Project administration, Funding acquisition. **Xiaozheng Chen:** Conceptualization, Methodology, Software, Validation, Writing – review & editing, Visualization, Funding acquisition. **Bastian Küppers:** Conceptualization, Methodology, Validation, Writing – review & editing. **Julius Lorenzo:** Investigation, Data curation, Writing – review & editing. **Abtin Magh-moumi:** Software, Data curation, Writing – review & editing, Visualization. **Matthias Schlaak:** Investigation, Writing – review & editing. **Eric Thor:** Software, Data curation, Writing – review & editing, Visualization. **Christian Nordmann:** Resources, Writing – review & editing, Funding acquisition. **Kathrin Greiff:** Supervision, Writing – review & editing, Funding acquisition.

Declaration of Competing Interest

The authors declared no potential conflicts of interest concerning the research, authorship, and/or publication of this article.

Data availability

Data will be made available on request.

Acknowledgments

We would like to thank STADLER Anlagenbau GmbH for providing the conveyor belt for T2 and Hündgen Entsorgungs GmbH & Co. KG for providing the LWP samples for T2. Many thanks to Christian de Ridder for his support in the practical investigations (T2).

Supplementary materials

Supplementary material associated with this article can be found, in the online version, at doi:10.1016/j.resconrec.2023.106873.

References

- Alassali, A., Picuno, C., Chong, Z.K., Guo, J., Maletz, R., Kuchta, K., 2021. Towards higher quality of recycled plastics: limitations from the material's perspective. *Sustainability* 13 (23), 13266. <https://doi.org/10.3390/su132313266>.
- Avio, C.G., Gorbi, S., Regoli, F., 2017. Plastics and microplastics in the oceans: from emerging pollutants to emerged threat. *Mar. Environ. Res.* 128, 2–11. <https://doi.org/10.1016/j.marenvres.2016.05.012>.
- Binder+Co AG. Service Products, 2022. <https://www.binder-co.com/1342/Service-Products#Plant-Improvements> (accessed August 16, 2022).
- Bradski, G., 2000. The OpenCV Library. Dr. Dobb's. *Journal of Software Tools*.
- Chen, X., Feil, A., 2019. Detection and classification of heterogeneous materials as well as small particles using NIR-spectroscopy by validation of algorithms. In: Beyerer, J., Puente León, F., Längle, T. (Eds.), OCM 2019 - Optical Characterization of Materials Conference Proceedings. KIT Scientific Publishing, pp. 63–77.
- Chen, X., Kroell, N., Althaus, M., Pretz, T., Pomberger, R., Greiff, K., 2023. Enabling mechanical recycling of plastic bottles with shrink sleeves through near-infrared spectroscopy and machine learning algorithms. *Resour. Conserv. Recycl.* 188, 106719. <https://doi.org/10.1016/j.resconrec.2022.106719>.
- Chen, X., Kroell, N., Dietl, T., Feil, A., Greiff, K., 2021a. Influence of long-term natural degradation processes on near-infrared spectra and sorting of post-consumer plastics. *Waste Manag.* 136, 213–218. <https://doi.org/10.1016/j.wasman.2021.10.006>.
- Chen, X., Kroell, N., Wickel, J., Feil, A., 2021b. Determining the composition of post-consumer flexible multilayer plastic packaging with near-infrared spectroscopy. *Waste Manag.* 123, 33–41. <https://doi.org/10.1016/j.wasman.2021.01.015>.
- Crespy, D., Bozonnet, M., Meier, M., 2008. 100 years of bakelite, the material of a 1000 uses. *Angew. Chem. Int. Ed. Engl.* 47 (18), 3322–3328. <https://doi.org/10.1002/anie.200704281>.
- Cudjoe, D., Zhu, B., Nketiah, E., Wang, H., Chen, W., Qianqian, Y., 2021. The potential energy and environmental benefits of global recyclable resources. *Sci. Total Environ.* 798, 149258. <https://doi.org/10.1016/j.scitotenv.2021.149258>.
- Curtis, A., Küppers, B., Möllnitz, S., Khodier, K., Sarc, R., 2021. Real time material flow monitoring in mechanical waste processing and the relevance of fluctuations. *Waste Manag.* 120 (1), 687–697. <https://doi.org/10.1016/j.wasman.2020.10.037>.
- Davidson, M.G., Furlong, R.A., McManus, M.C., 2021. Developments in the life cycle assessment of chemical recycling of plastic waste – a review. *J. Clean. Prod.* 293, 126163. <https://doi.org/10.1016/j.jclepro.2021.126163>.
- Deutsches Institut für Normung e.V. In: DIN 1310: Zusammensetzung von Mischphasen, 1984. *Gasgemische, Lösungen, Mischkristalle*; Begriffe, Formelzeichen.
- Driscoll, R., Agarwal, S., Laforsch, C., 2020. Plastics: from a success story to an environmental problem and a global challenge. *Global challenges* (Hoboken, NJ) 4 (6), 2000026. <https://doi.org/10.1002/gch2.202000026>.
- EVK Kerschhagl GmbH. EVK HELIOS NIR G2-320: smart hyperspectral imaging camera, 2022a. <https://www.evk.biz/en/products/hyperspectral-camera/evk-helios-nir-g2-320-class/> (accessed December 11, 2022).
- EVK Kerschhagl GmbH. EVK SQUALAR: software Tool for the qualitative and quantitative analysis, 2022b. <https://www.evk.biz/en/products/analysis-software-tool/evk-squalar/> (accessed December 11, 2022).
- Fahrmeir, L., Kneib, T., Lang, S., Marx, B., 2013. *Regression: Models, Methods and Applications*. Springer, Berlin, Heidelberg.
- Feil, A., Kroell, N., Pretz, T., Greiff, K., 2021. Anforderungen an eine effiziente technologische Behandlung von Post-Consumer Verpackungsmaterialien in Sortieranlagen. *Müll und Abfall* 21 (7), 362–370. <https://doi.org/10.37307/j.1863-9763.2021.07.04>.
- Feil, A., Pretz, T., 2020. Mechanical recycling of packaging waste. In: Letcher, T.M. (Ed.), *Plastic Waste and recycling: Environmental impact, Societal issues, prevention, and*

- Solutions*. Academic Press, Amsterdam, San Diego, Cambridge, MA, Kidlington, pp. 283–319.
- Friedrich, K., Koinig, G., Pomberger, R., Vollprecht, D., 2022. Qualitative analysis of post-consumer and post-industrial waste via near-infrared, visual and induction identification with experimental sensor-based sorting setup. *MethodsX* 9, 101686. <https://doi.org/10.1016/j.mex.2022.101686>.
- Geyer, R., Jambeck, J.R., Law, K.L., 2017. Production, use, and fate of all plastics ever made. *Sci. Adv.* 3 (7), e1700782 <https://doi.org/10.1126/sciadv.1700782>.
- Harris, C.R., Millman, K.J., van der Walt, S.J., Gommers, R., Virtanen, P., Cournapeau, D., et al., 2020. Array programming with NumPy. *Nature* 585 (7825), 357–362. <https://doi.org/10.1038/s41586-020-2649-2>.
- Hunter, J.D., 2007. Matplotlib: a 2D graphics environment. *Comput. Sci. Eng.* 9 (3), 90–95. <https://doi.org/10.1109/MCSE.2007.55>.
- Initiative „Mülltrennung wirkt“, 2021. „Ein Jahr Initiative „Mülltrennung wirkt“: von den Herausforderungen zum Erfolg: duale Systeme bilden eine starke Allianz für mehr Aufklärung. Müll und Abfall (7), 352–360. <https://doi.org/10.37307/j.1863-9763.2021.07.03>.
- ISO, 2022. ISO 5725. International Organization for Standardization, Geneva accessed October 22, 2022.
- Jambeck, J.R., Geyer, R., Wilcox, C., Siegler, T.R., Perryman, M., Andrady, A., et al., 2015. Marine pollution. Plastic waste inputs from land into the ocean. *Science* 347 (6223), 768–771. <https://doi.org/10.1126/science.1260352>.
- Kleinhans, K., Küppers, B., Hernández Parrodi, J.C., Raegert, K., Dewulf, J., de Meester S, et al., 2022. Challenges faced during a near-infrared-based material flow characterization study of commercial and industrial waste. In: Greiff, K., Wotruba, H., Feil, A., Kroell, N., Chen, X., Gürsel, D., et al. (Eds.), 9th Sensor-Based Sorting & Control, 13.04.2022 - 14.04.2022: Aachen; 2022.
- Kroell, N., 2021. imea: a Python package for extracting 2D and 3D shape measurements from images. *J. Open Source Softw.* 6 (60), 3091 <https://doi.org/10.21105/joss.03091>.
- Kroell, N., Chen, X., Greiff, K., Feil, A., 2022a. Optical sensors and machine learning algorithms in sensor-based material flow characterization for mechanical recycling processes: a systematic literature review. *Waste Manag.* 149, 259–290. <https://doi.org/10.1016/j.wasman.2022.05.015>.
- Kroell, N., Chen, X., Maghmoumi, A., Koenig, M., Feil, A., Greiff, K., 2021. Sensor-based particle mass prediction of lightweight packaging waste using machine learning algorithms. *Waste Manag.* 136, 253–265. <https://doi.org/10.1016/j.wasman.2021.10.017>.
- Kroell, N., Dietl, T., Maghmoumi, A., Chen, X., Küppers, B., Feil, A., et al., 2022b. Assessment of sensor-based sorting performance for lightweight packaging waste through sensor-based material flow monitoring: concept and preliminary results. In: Greiff, K., Wotruba, H., Feil, A., Kroell, N., Chen, X., Gürsel, D., et al. (Eds.), 9th Sensor-Based Sorting & Control, 13.04.2022 - 14.04.2022: Aachen; 2022.
- Küppers, B., Chen, X., Seidler, I., Friedrich, K., Raulf, K., Pretz, T., et al., 2019a. Influences and consequences of mechanical delabelling on pet recycling. *Detritus* 06 (0), 1. <https://doi.org/10.31025/2611-4135/2019.13816>. - June 2019.
- Küppers, B., Schloegl, S., Oreski, G., Pomberger, R., Vollprecht, D., 2019b. Influence of surface roughness and surface moisture of plastics on sensor-based sorting in the near infrared range. *Waste management & research the journal of the International Solid Wastes and Public Cleansing Association. ISWA* 37 (8), 843–850. <https://doi.org/10.1177/0734242X19855433>.
- Küppers, B., Schlögl, S., Kroell, N., Radkohl, V., et al., 2022. Relevance and challenges of plant control in the pre-processing stage for enhanced sorting performance. In: Greiff, K., Wotruba, H., Feil, A., Kroell, N., Chen, X., Gürsel, D., et al. (Eds.), 9th Sensor-Based Sorting & Control, 13.04.2022 - 14.04.2022: Aachen; 2022.
- Länderarbeitsgemeinschaft Abfall, 2001. Richtlinie für das Vorgehen bei physikalischen und chemischen Untersuchungen im Zusammenhang mit der Verwertung/Beseitigung von Abfällen (LAGA PN 98).
- Maisel, F., Chancerel, P., Dimitrova, G., Emmerich, J., Nissen, N.F., Schneider-Ramelow, M., 2020. Preparing WEEE plastics for recycling – How optimal particle sizes in pre-processing can improve the separation efficiency of high quality plastics. *Resour. Conserv. Recycl.* 154, 104619 <https://doi.org/10.1016/j.resconrec.2019.104619>.
- McKinney, W., 2010. Data structures for statistical computing in Python. In: Stéfan van der Walt, Jarrod Millman. *Proceedings of the 9th Python in Science Conference*.
- Moore, C.J., 2008. Synthetic polymers in the marine environment: a rapidly increasing, long-term threat. *Environ. Res.* 108 (2), 131–139. <https://doi.org/10.1016/j.envres.2008.07.025>.
- Nielsen, T.D., Hasselbalch, J., Holmberg, K., Strippl, J., 2020. Politics and the plastic crisis: a review throughout the plastic life cycle. *WIREs Energy Environ.* 9 (1) <https://doi.org/10.1002/wene.360>.
- Pearson, K.VII, 1895. Note on regression and inheritance in the case of two parents. *Proc. Royal Soc. London* 58 (347–352), 240–242. <https://doi.org/10.1098/rsp1.1895.0041>.
- Pedregosa, F., Varoquaux, G., Gramfort, A., Michel, V., Thirion, B., Grisel, O., et al., 2011. Scikit-learn: machine learning in Python. *J. Open Source Softw.* 12, 2825–2830.
- Pellenc ST SAS. MISTRAL+ CONNECT, 2022. <https://www.pellencst.com/products> (accessed August 16, 2022).
- Plastic Europe. The circular economy for plastics: a European overview, 2022. <https://plasticseurope.org/knowledge-hub/the-circular-economy-for-plastics-a-european-overview-2/> (accessed May 27, 2022).
- REDWAVE. REDWAVE mate, 2022. <https://redwave.com/en/products?setLang=1> (accessed August 16, 2022).
- Rosato, Strandburg, Prinz, Swendsen, 1987. Why the Brazil nuts are on top: size segregation of particulate matter by shaking. *Phys. Rev. Lett.* 58 (10), 1038–1040. <https://doi.org/10.1103/PhysRevLett.58.1038>.
- Schlögl, S., Küppers, B., et al., 2022. Quantifying the delabelling performance using sensor-based material flow monitoring. In: Greiff, K., Wotruba, H., Feil, A., Kroell, N., Chen, X., Gürsel, D., et al. (Eds.), 9th Sensor-Based Sorting & Control, 13.04.2022 - 14.04.2022: Aachen; 2022.
- Sesotec GmbH. Recycling sorting systems with conveyor belt, 2022. <https://www.sesotec.com/emea/en/products/groups/recycling-sorting-systems-with-conveyor-belt> (accessed August 16, 2022).
- Shen, M., Huang, W., Chen, M., Song, B., Zeng, G., Zhang, Y., 2020. Microplastic crisis: un-ignorable contribution to global greenhouse gas emissions and climate change. *J. Clean. Prod.* 254, 120138 <https://doi.org/10.1016/j.jclepro.2020.120138>.
- STEINERT GmbH. STEINERT.view, 2022. <https://steinertglobal.com/de/steinert-digit-al/dashboard-view/> (accessed August 16, 2022).
- The pandas development team. pandas-dev/pandas: pandas: zenodo, 2020.
- TOMRA System ASA. TOMRA Insight, 2022. <https://www.tomra.com/en/solutions/waste-metal-recycling/tomra-insight> (accessed August 16, 2022).
- van der Walt, S., Schönberger, J.L., Nunez-Iglesias, J., Boulogne, F., Warner, J.D., Yager, N., et al., 2014. scikit-image: image processing in Python. *PeerJ* 2, e453. <https://doi.org/10.7717/peerj.453>.
- Virtanen, P., Gommers, R., Oliphant, T.E., Haberland, M., Reddy, T., Cournapeau, D., et al., 2020. SciPy 1.0: fundamental algorithms for scientific computing in Python. *Nat. Methods* 17, 261–272. <https://doi.org/10.1038/s41592-019-0686-2>.
- Waskom, M.L., 2021. seaborn: statistical data visualization. *J. Open Source Softw.* 6 (60), 3021. <https://doi.org/10.21105/joss.03021>.
- Zheng, J., Suh, S., 2019. Strategies to reduce the global carbon footprint of plastics. *Nat. Clim. Chang.* 9 (5), 374–378. <https://doi.org/10.1038/s41558-019-0459-z>.